coatings

MDPI

Article

Deformation Behavior and Processing Map of $AlCoCrFeNiTi_{0.5}$ High-Entropy Alloy at High Temperature

Xinbin Liu [1,2], Tiansheng Li [1,2], Yong Wang [1,*], Xianghua Kong [3,*] and Chenyang Zhao [1]

[1] School of Intelligent Manufacturing and Mechanical Engineering, Hunan Institute of Technology, Hengyang 421002, China; liuxinbin@hnit.edu.cn (X.L.); litiansheng@hnit.edu.cn (T.L.); zhaochya@163.com (C.Z.)
[2] Modern Engineering Technology Practice Teaching Department, Hunan Institute of Technology, Hengyang 421002, China
[3] Hunan Tieying New Materials Co., Ltd., Yueyang 414000, China
* Correspondence: wangyong@hnit.edu.cn (Y.W.); kongxianghua685@163.com (X.K.)

Abstract: $AlCoCrFeNiTi_{0.5}$ high-entropy alloy (HEA) shows excellent properties in hardness and corrosion resistance. $AlCoCrFeNiTi_{0.5}$ HEA was prepared using a non-consumable vacuum arc furnace. Hot-deformation behavior of $AlCoCrFeNiTi_{0.5}$ HEA was explored under 1073–1373 K with a strain rate between 0.001 and 1 s^{-1} using a Gleeble-3800 thermomechanical simulator. The constitutive equation was established using the Arrhenius model, and the deformation activation energy and material constant were obtained. The processing map of HEA within 0.3–0.6 deformation was drawn according to dynamic material model (DMM). The results show that the hot-deformation process of HEA is dominated by work hardening combined with dynamic recovery, and dynamic recrystallization. The flow stress of HEA is significantly affected by deformation temperature and strain rate. The constitutive equation was constructed and verified, and the correlation coefficient of R^2 = 0.9873 indicated that the constitutive equation can be used to accurately predict the flow stress of HEA. The processing map of HEA shows that the optimal hot-working process parameters are in the range of temperature 1150–1300 K and strain rate 0.002–0.05 s^{-1}. This work will provide theoretical guidance for the hot-processing of HEA, which effectively promotes the application of the HEA in industry.

Keywords: hot-deformation behavior; high-entropy alloy; constitutive equation; processing map

Citation: Liu, X.; Li, T.; Wang, Y.; Kong, X.; Zhao, C. Deformation Behavior and Processing Map of $AlCoCrFeNiTi_{0.5}$ High-Entropy Alloy at High Temperature. *Coatings* **2023**, *13*, 1811. https://doi.org/10.3390/coatings13101811

Academic Editor: Amalraj Marshal

Received: 26 September 2023
Revised: 19 October 2023
Accepted: 20 October 2023
Published: 22 October 2023

1. Introduction

High-entropy alloy (HEA) is a new kind of alloy that contain more than five principal elements in equal or near equal atomic percent. It has attracted increasing attentions because of unique compositions, microstructures, and properties [1,2], such as high strength, high ductility, wear resistance, corrosion resistance, and temperature resistance [3,4]. Due to the interaction of different elements, HEA exhibit a composite effect. The grain shape, grain diameter and grain boundary of HEA may be affected by some elements, which change the macroscopic properties.

CoCrFeNi HEA is composed of face-centered cubic (FCC) phases, which have been investigated by numerous researchers [5–7]. CoCrFeNi HEA exhibits excellent plasticity, toughness, and fracture toughness, but its application was limited because of low strength. Lots of studies have been conducted to improve the strength of CoCrFeNi HEA. The comprehensive performance of CoCrFeNi HEA can be improved by introduced body-centered cubic phases (BCC), such as Al, Ti, Cu, Mn and others. It has been reported that the hardness can be increased by adding Al and the corrosion resistance can be improved by adding Ti [8–12]. Qin et al. [13] reported that the yield strength and fracture strength of CoCrFeMnNi HEA was significantly improved by Mo addition. Mohamed et al. [14] investigated the effect of Cu addition on mechanical properties of AlCoCrFeNi HEA; they showed that

the hardness decreased significantly with an increase in Cu content, the hardness decreases from 403 HV to 191 HV when the Cu content increases from 5 wt% to 20 wt%, whereas the compressive strength increases form 400.034 MPa to 599.527 MPa when the Cu content increases from 5 wt% to 15 wt%. Zhao et al. [15,16] studied the microstructure evolution, hardness and wear resistance of HEMB-Ni_2B composite coating via first principle methods; the results show that the synergistic effect between the superhardness of HEMB and the large plastic deformation ability of Ni_2B can significantly improve the wear resistance of HEMB-Ni_2B coatings, with a friction coefficient as low as 0.13. Similar investigations have been also reported in references [15–23]. Yu et al. [17] demonstrated that the structure of $Al_xCoCrFeNi$ HEA transforms from a single FCC phase to an FCC + BCC dual phase with the increases in Al contents. Meanwhile, the hardness is improved by 146% with a 0.9% Al addition compared with CoCrFeNi. Zhang et al. [19] found that the surface roughness is the smallest of $CoCrFeNiAl_X$ (x = 0, 0.6, 1) with a 0.6 wt% Al addition. Wu et al. [20] reported that the transition temperature from order to disorder in $FeCoNiAl_{1-x}Ti_x$ decreases with the increase in Ti content. Zhang et al. [22] showed that the average microhardness of the $AlCoCrFeNiTi_{0.5}$ HEA coating reached 989 HV, which was 32% higher than AlCoCrFeNi and reduced wear by 85%. The addition of Ti increased the number of reinforcement phases in the alloy, which contributed to the formation of eutectic and amplitude-modulated decomposition structures, and this structure showed significant changes in performance.

Due to the mixing effect of HEA, adding different elements will have different effects, resulting in significant differences in microstructure and properties. Moreover, the inherent characteristics and casting defects of HEA, high resistance and poor plasticity during hot-working, cracking during forging and hot-rolling process, and other problems restrict the application of HEA [24,25]. The studies on HEA mainly focus on the composition, microstructure, and mechanical properties, whereas there are few studies on high-temperature deformation behavior [26,27]. So, the hot-deformation behavior and mechanism of HEA should be investigated in detail, which are meaningful for the production of bulk defect free HEA.

The combination of the dynamic material model (DMM) processing diagram and microstructure after high-temperature deformation can effectively describe the relationship between high-temperature deformation parameters and microstructure evolution [24], which is used to distinguish the safe and dangerous zones during the high-temperature plastic deformation process [28,29]. The hot-compression experiments of $AlCoCrFeNiTi_{0.5}$ under different conditions (deformation temperature, strain rate) were conducted, and the deformation behavior at high temperature was analyzed. The flow stress constitutive equation within 0.1–0.7 deformation was established according to the Arrhenius model. The processing map of $AlCoCrFeNiTi_{0.5}$ within 0.3–0.6 deformation was drawn according to DMM. This paper aims at providing theoretical basis for the formulation and optimization of HEA hot-deformation process parameters, which is beneficial to solving the problems including hot-work difficulties and cracking during the hot-processing of HEA.

2. Experiments

The tested material is as-cast $AlCoCrFeNiTi_{0.5}$ HEA. The ingot was smelted using a WK-II non-consumable vacuum arc furnace (BNTET, Henan, China) with Al, Co, Cr, Fe, Ni, and Ti as raw materials (purity > 99.9%). During the melting process, Al, Co, Cr, Fe, Ni, and Ti are prepared in an atom ratio of 1:1:1:1:1:0.5 in order to reduce the volatilization of low-melting-point alloys before melting; the alloys are gradually placed in a copper crucible in the order of melting point from low to high. The ingot was repeatedly melted 5–6 times to ensure the uniformity of chemical composition. The chemical composition of the ingot is shown in Table 1.

Table 1. Chemical composition of $AlCoCrFeNiTi_{0.5}$ HEA (atom%).

Element	Al	Co	Cr	Fe	Ni	Ti
Content	17.69	18.21	18.60	18.63	18.28	8.59

The ingot was processed into a cylinder with 8 mm in diameter and 10 mm in height for hot-compression experiments. Single-pass compression tests were carried out using the Gleeble-3800 thermomechanical simulator (DSI, Albany, NY, USA). The schematic diagram of the hot-compression experiment is shown in Figure 1. The specimens were heated to 1423 K at a rate of 10 K·s^{-1} and held for 3 min to eliminate the internal temperature gradient, and cooled to deformation temperature at a rate of 3 K·s^{-1}. The deformation temperature was set as 1073 K, 1173 K, 1273 K or 1373 K. The strain rate was set as 0.001 s^{-1}, 0.01 s^{-1}, 0.1 s^{-1} or 1 s^{-1}; the total deformation is 70%. When the temperature was reached, the specimens were held for 30 s, and then single-pass compressing tests were carried out and repeated for all the experiments under different temperature. The crystal structure of the sample was tested using an XRD-6100 Lab X-ray diffraction analyzer (SHIMADZU, Kyoto, Japan) with CuK α Ray, λ = 0.15406 nm. The working current is 30 mA, working voltage is 40 kV, scanning angle range is 20–90°, and scanning speed is 2 (°)/min. The microstructure of $AlCoCrFeNiTi_{0.5}$ HEA is analyzed using the OLYMPUS BX51M optical microscope (OM, Olympus Corporation, Tokyo, Japan) after electropolishing with 4% fluoroboric acid.

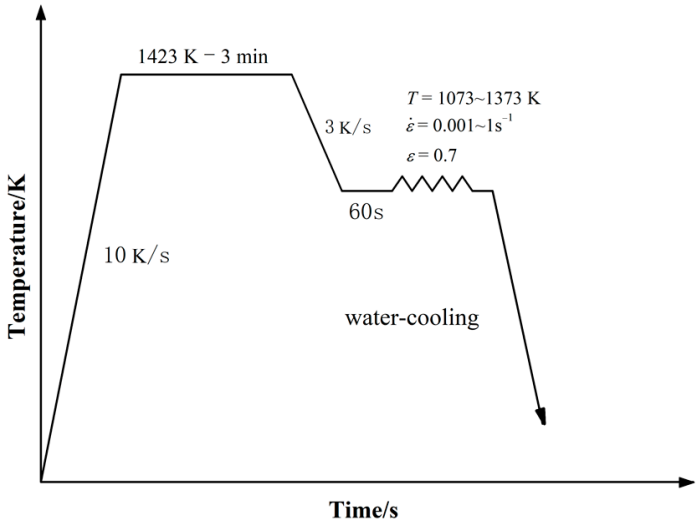

Figure 1. Schematic diagram of hot-compression experiment.

3. Results

3.1. Microstructure

The XRD patterns of the specimens of $AlCoCrFeNiTi_{0.5}$ HEA are shown in Figure 2; it can be inferred that the main components are FCC and BCC phases. The diffraction peaks of the FCC phase are crystal face (111), (200), and (220) with a structure of [Fe, Ni] solid solution. The lattice constant of FCC is 0.35807 nm, and the spatial group belongs to the Fm-3m (225) spatial structure. The diffraction peaks of BCC phase are crystal face (100), (110), (200), and (211) with a structure of [Fe, Cr] solid solution. The lattice constant of FCC is 0.28719 nm, and the spatial group belongs to the Im-3m (229) spatial structure. The microstructure of $AlCoCrFeNiTi_{0.5}$ HEA is detected by OM, as shown in Figure 3, where there are two phases, which should belong to the BCC and FCC phase according to the result in Figure 2.

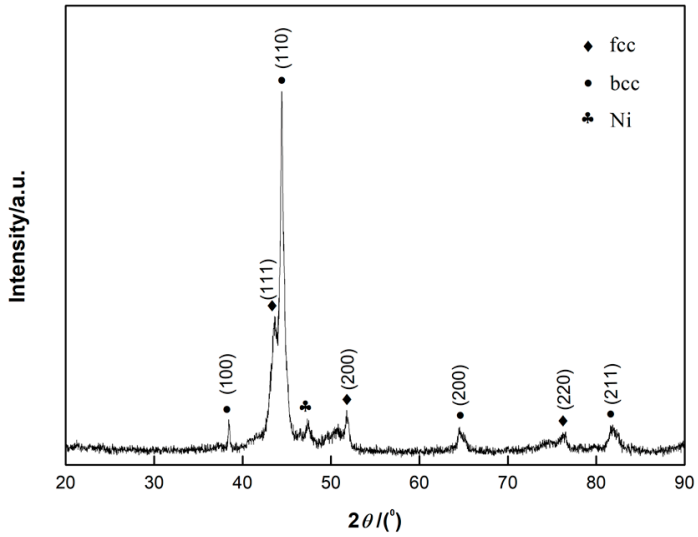

Figure 2. XRD patterns of $AlCoCrFeNiTi_{0.5}$ HEA.

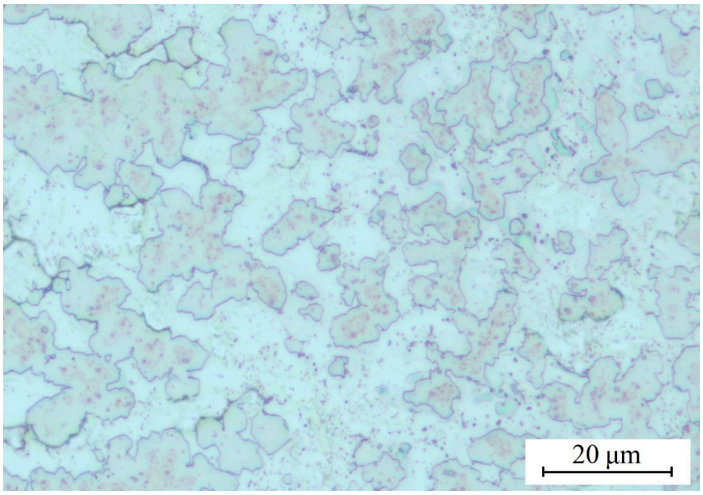

Figure 3. Microstructure of $AlCoCrFeNiTi_{0.5}$ HEA.

3.2. Analysis of Stress–Strain Curve

Figure 4 shows the flow stress–strain curve of $AlCoCrFeNiTi_{0.5}$ HEA under different conditions. It can be observed that the flow stress is significantly affected by temperature and strain rate. The flow stress increases with the increase in strain rate and the decrease in temperature. During the hot-deformation process, both work hardening and dynamic softening mechanisms work simultaneously [30]. At the initial stage, the stress increases quickly with the increase in deformation, and the increase rate shows a gradual slowing trend before reaching the peak value. This indicates that this stage belongs to the dynamic recovery process. The hardworking plays the main role, where dislocation multiplication hinders the movement, the softening effect caused by dislocation movement is insufficient to offset the hardening effect caused by the increase in dislocation density, resulting in a rapid increase in flow stress and a significant increase in deformation resistance. Subsequently, dynamic recovery occurs, and the dislocations recombine and disappear, which makes the stress reach the peak value gradually. After that, the stress decreases gradually until it reaches a steady state with the increase in deformation. The dynamic softening mechanisms plays the main role at this stage. The synergy effect of dynamic recovery and dynamic recrystallization is stronger than that of work hardening, and the stress decreases gradually and reaches the steady state when it reaches the equilibrium state [31]. When the strain rate is constant, the dynamic recrystallization behavior becomes more obvious with

the increase in deformation temperature, and the peak value of flow stress correspondingly decreases. With the increase in deformation temperature, the thermal activation effect of deformation increases, which enhances the mobility of grain boundaries, promoting the dynamic recrystallization nucleation, grain growth, and dislocation annihilation. This will reduce the flow stress [32]. When the deformation temperature is constant, the nucleation and growth of recrystallized grains become more complete with the decrease in strain rate, contributing fully to dynamic recrystallization. The interaction between dislocations leads to a sharp increase in dislocation density, which increases the deformation storage energy, leading to a decrease in the critical temperature of recrystallization and a corresponding increase in the degree of dynamic recrystallization.

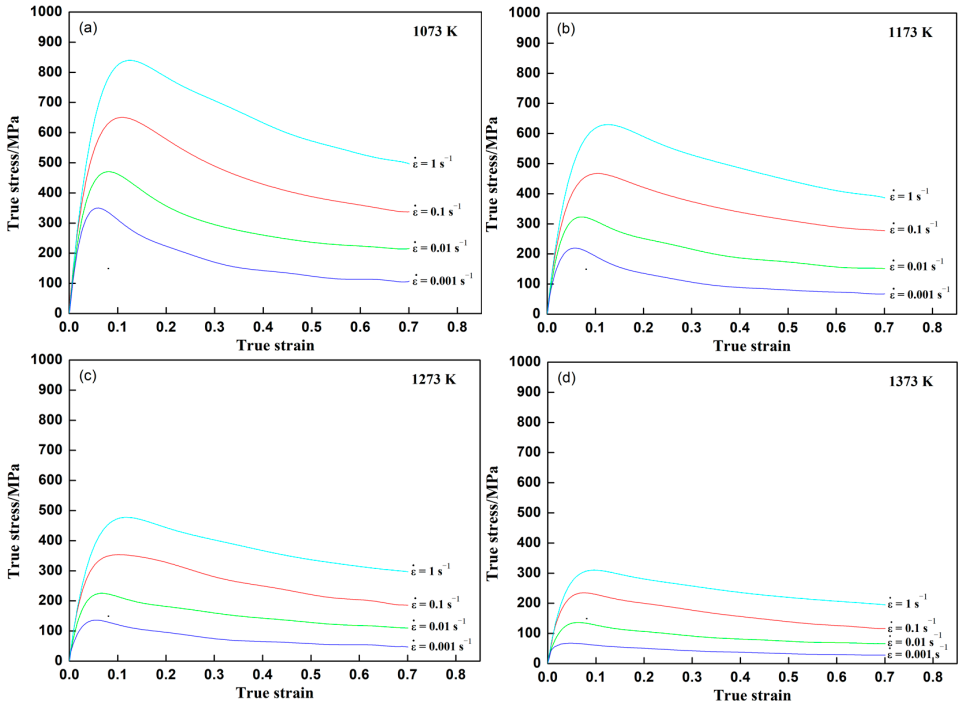

Figure 4. Flow stress–strain curve of $AlCoCrFeNiTi_{0.5}$ HEA under different conditions: (**a**) 1073 K, (**b**) 1173 K, (**c**) 1273 K, (**d**) 1373 K.

3.3. Establishment of Constitutive Equation

It has been reported that the constitutive equation could be used to exhibit the relationship between flow stress and deformation parameters during the deformation process of alloys [33,34]. The constitutive equation for $AlCoCrFeNiTi_{0.5}$ HEA can be expressed with the following equations [35,36]:

$$\dot{\varepsilon} = A_1 \sigma^{n_1} \exp\left(-\frac{Q}{RT}\right), \sigma < 0.8 \quad (1)$$

$$\dot{\varepsilon} = A_2 \exp(\beta\sigma) \exp\left(-\frac{Q}{RT}\right), \sigma > 1.2 \quad (2)$$

$$\dot{\varepsilon} = A[\sinh(\alpha\sigma)]^n \exp\left(-\frac{Q}{RT}\right) \quad (3)$$

where Q is activation energy (kJ·mol^{-1}), R is the universal gas constant (8.314 J·mol^{-1}·K^{-1}), σ is flow stress (MPa), $\dot{\varepsilon}$ is strain rate (s^{-1}), T is deformation temperature (K), A_1, A_2 and A_3 are material constants, n and n_1 are stress exponents, and α is stress factor ($\alpha = \beta/n_1$, MPa^{-1}). It should be noticed that Equation (3) is suitable for any condition.

Zener and Hollomon used parameter Z to describe the effects of temperature and strain rate on deformation behaviors [37]:

$$Z = \dot{\varepsilon} \exp\left(\frac{Q}{RT}\right) = A[\sinh(\alpha\sigma)]^n \tag{4}$$

The value of α, n, Q and A can be calculated by Equations (1)–(4), and then establish the constitutive equation under different deformation condition. In this paper, the constitutive equation is obtained when the strain is 0.2, and the stress at different conditions is shown in Table 2.

Table 2. Stress of $AlCoCrFeNiTi_{0.5}$ HEA under different conditions with 0.2 deformation (MPa).

Strate Rate, s^{-1}	Deformation Temperature, K			
	1073	1173	1273	1373
0.001	208.73	135.38	100.67	35.98
0.01	356.08	250.93	204.53	106.53
0.1	577.51	420.55	356.68	199.74
1	783.40	589.19	480.24	280.40

By taking the logarithm of both sides of Equations (1) and (2), Equations (5) and (6) can be expressed as follows:

$$\ln \dot{\varepsilon} = \ln A_1 + n_1 \ln \sigma - \frac{Q}{RT} \tag{5}$$

$$\ln \dot{\varepsilon} = \ln A_2 + \beta\sigma - \frac{Q}{RT} \tag{6}$$

By performing a linear fitting on ln$\dot{\varepsilon}$-lnσ and ln$\dot{\varepsilon}$-σ, and finding the reciprocal of the slope of the line, the value of n_1 and β can be obtained. The value of α can be calculated by $\alpha = \beta/n_1$. As shown in Figure 5a,c, $n_1 = 6.05$, $\beta = 0.026$, and $\alpha = 0.0041$.

Equation (7) of Q can be obtained by taking the logarithm of both sides of Equation (3) and finding the partial differential:

$$Q = R\frac{\partial \ln[\sinh(\alpha\sigma)]}{\partial(1/T)}\bigg|_{\dot{\varepsilon}} \frac{\partial \ln \dot{\varepsilon}}{\partial \ln[\sinh(\alpha\sigma)]}\bigg|_{T} = Rbn \tag{7}$$

The relationship between ln[sinh($\alpha\sigma$)]-$1/T$, and ln$\dot{\varepsilon}$-ln[sinh($\alpha\sigma$)] is shown in Figure 5c,d. it can be inferred that $b = 7948.35$, $n = 3.25$, and $Q = 218.36$ kJ/mol.

By taking the logarithm of both sides of Equation (4), Equation (8) can be expressed as follows:

$$\ln Z = \ln \dot{\varepsilon} + \frac{Q}{RT} = \ln A + n \ln[\sinh(\alpha\sigma)] \tag{8}$$

Perform linear fitting on ln$Z$-ln[sinh($\alpha\sigma$)], the reciprocal of the slope of the line is ln$A = 17.42$, and $A = 3.68 \times 107$, as shown in Figure 5e.

Take the values of α, n, Q and A into Equation (3), the constitutive equation (strain = 0.2) is obtained.

$$\dot{\varepsilon} = 2.78 \times 10^7 [\sinh(0.0041\sigma)]^{3.25} \exp\left(-\frac{218359}{RT}\right) \tag{9}$$

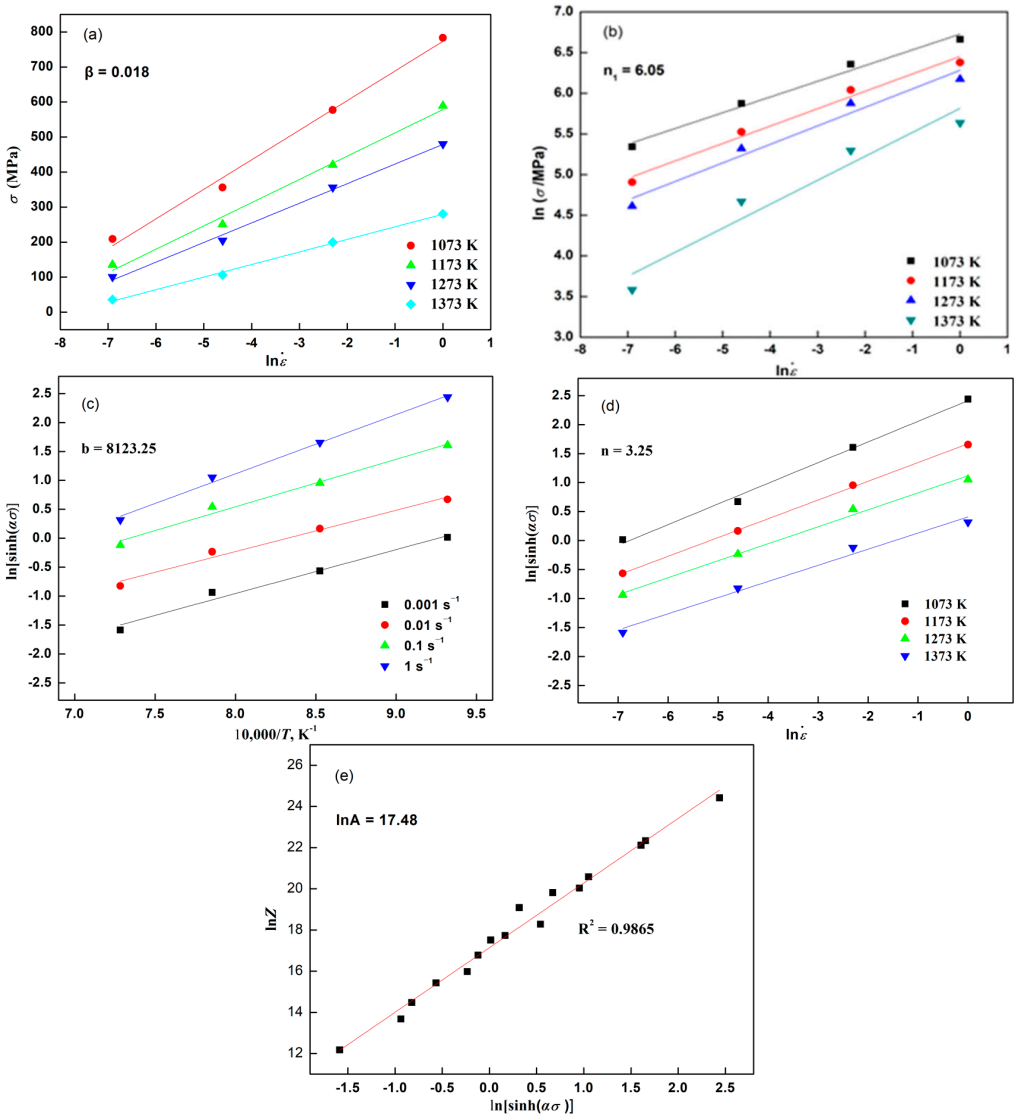

Figure 5. Parameter fitting relationship of of $AlCoCrFeNiTi_{0.5}$ HEA with 0.2 deformation. (**a**) ln$\dot{\varepsilon}$-lnσ, (**b**) ln$\dot{\varepsilon}$-σ, (**c**) ln[sinh($\alpha\sigma$)]-1/T, (**d**) ln$\dot{\varepsilon}$-ln[sinh($\alpha\sigma$)], (**e**) ln$Z$-ln[sinh($\alpha\sigma$)].

It has been reported that the rheological characteristics of an alloy can be described by the relationship between strain and material constant. The values of α, n, Q and ln$A$ under different deformation conditions are shown in Table 3. The material constant is represented as a polynomial function of the strain, which can more accurately reflect the relationship between the material constant and the strain, and the corresponding results are shown in Figure 6. The correlation coefficient is higher than 0.9760, which indicates that the fitting effect is good. The relationship between stress and material constant can be obtained by combining Equations (3) and (4). Combining the calculated material constants with strain polynomial fitting results, the constitutive equation of $AlCoCrFeNiTi_{0.5}$ can be expressed as follows.

$$\begin{cases} \sigma = \frac{1}{\alpha}\ln\left\{\left(\frac{Z}{A}\right)^{\frac{1}{n}} + \left[\left(\frac{Z}{A}\right)^{\frac{2}{n}} + 1\right]^{\frac{1}{2}}\right\} \\ Z = \dot{\varepsilon}\exp\left(\frac{Q}{RT}\right) \\ \alpha = -0.3303\varepsilon^6 + 0.6176\varepsilon^5 - 0.3993\varepsilon^4 + 0.0951\varepsilon^3 \\ \quad -0.0036\varepsilon^2 + 0.0058\varepsilon + 0.0028 \\ n = -166.77\varepsilon^6 + 467.09\varepsilon^5 - 505.70\varepsilon^4 + 255.07\varepsilon^3 \\ \quad -51.47\varepsilon^2 - 1.87\varepsilon + 4.32 \\ Q = -53062.40\varepsilon^6 + 131273.29\varepsilon^5 - 127864.15\varepsilon^4 \\ \quad +61133.49\varepsilon^3 - 14029.85\varepsilon^2 + 1015.05\varepsilon + 256.35 \\ \ln A = 6902.09\varepsilon^6 - 17741.01\varepsilon^5 + 18090.01\varepsilon^4 \\ \quad -9345.30\varepsilon^3 + 2614.99\varepsilon^2 - 398.61\varepsilon + 43.03 \end{cases} \quad (10)$$

Table 3. Material constant of $AlCoCrFeNiTi_{0.5}$ HEA under different deformation condition.

ε	α	n	ln$A$	Q/(kJ·mol^{-1})
0.10	0.0034	5.6	21.88	266.725
0.15	0.0038	3.84	17.79	245.83
0.20	0.0041	3.49	17.42	218.359
0.25	0.0044	3.3	15.85	205.404
0.30	0.0049	3.08	14.65	194.146
0.35	0.0051	2.899	14.05	186.814
0.40	0.0054	2.85	13.71	183.435
0.45	0.0056	2.83	13.45	182.321
0.50	0.0058	2.84	13.31	178.158
0.55	0.0062	2.77	13.37	179.514
0.60	0.0064	2.76	13.62	182.07
0.65	0.0066	2.79	13.52	180.963
0.70	0.0068	2.76	13.5	181.57

3.4. Verification of Constitutive Equation

In order to verify the accuracy of the constitutive equation, the stress of $AlCoCrFeNiTi_{0.5}$ HEA under different strain rates is calculated according to Equation (10); the corresponding results are shown in Figure 7. It can be concluded that the theoretical calculation values and experimental values are highly consistent when the strain rate is 0.001 s^{-1}, 0.01 s^{-1} and 0.1 s^{-1}. However, there is a significant deviation between the theoretical calculation value and the experimental value when the strain rate is 1 s^{-1} at 1073 K and 1373 K. Figure 8 shows the comparison between the theoretical and experimental values of flow stress. The slope of the curve is 0.9757, and the correlation coefficient is 0.9873, which indicates that the constitutive equation can accurately predict the flow stress of $AlCoCrFeNiTi_{0.5}$ HEA.

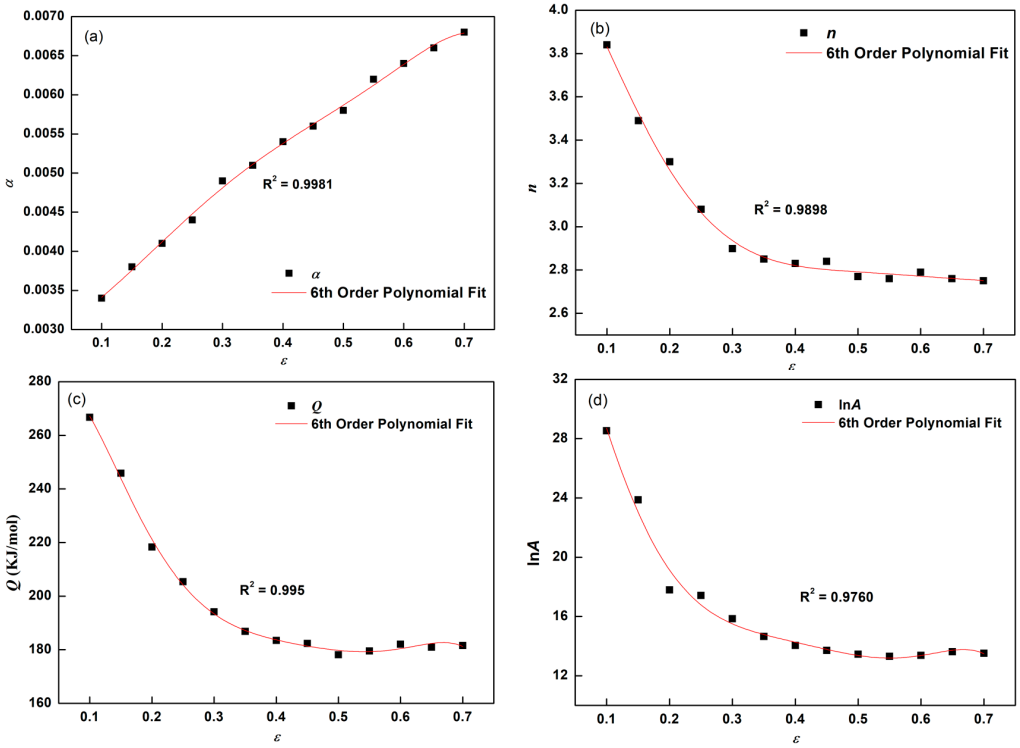

Figure 6. Relationship curve between stress and (**a**) α, (**b**) n, (**c**) Q, (**d**) ln$A$.

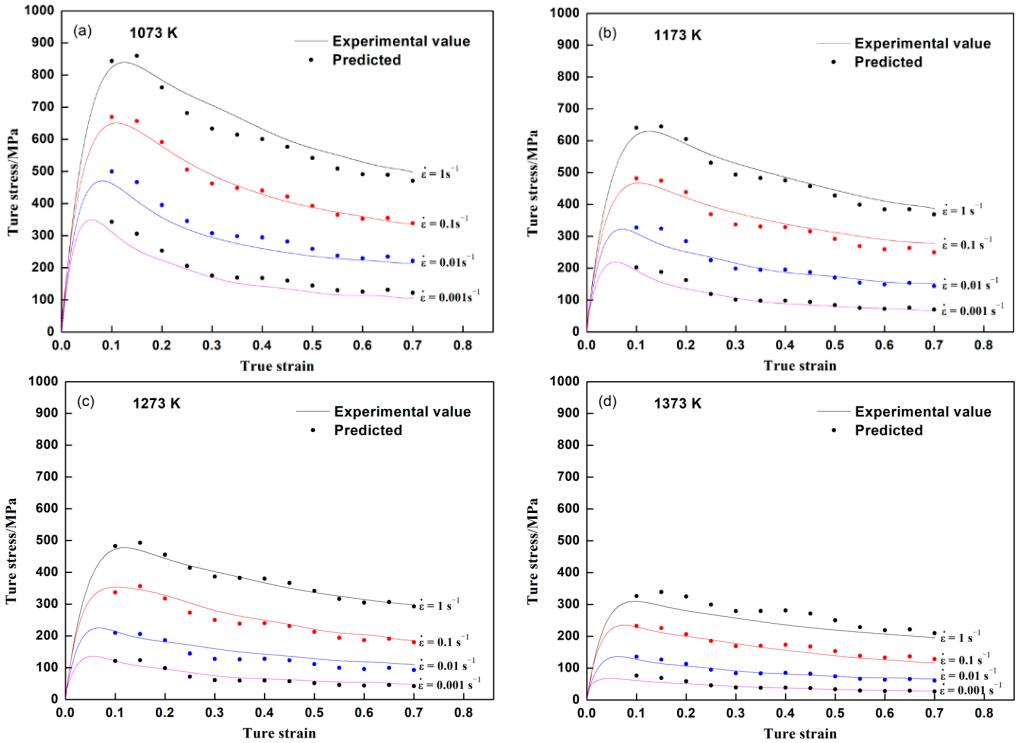

Figure 7. Comparison between experimental and theoretical values of stress under different deformation conditions: (**a**) 1073 K, (**b**) 1173 K, (**c**) 1273 K, (**d**) 1373 K.

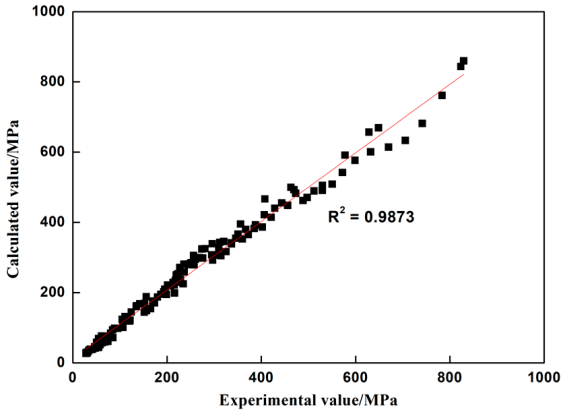

Figure 8. Contrast effect between the theoretical and experimental values of flow stress.

3.5. Processing Map

It has been reported that the processing map based on dynamic material model (DMM) is widely used to investigate the deformation behavior of materials at high temperature [38]. During the thermal deformation process, the total energy (P) absorbed by the material can be divided into two parts: the energy consumed by plastic deformation (G), and the energy consumed by microstructure transformation (J), following Equation (11) [39].

$$P = G + J = \sigma \cdot \dot{\varepsilon} = \int_0^{\dot{\varepsilon}} \sigma \mathrm{d}\dot{\varepsilon} + \int_0^{\sigma} \dot{\varepsilon} \mathrm{d}\sigma \tag{11}$$

The relationship between flow stress and stain rate can be expressed by Equation (12) [40]:

$$\sigma = K(\dot{\varepsilon})^m \tag{12}$$

where K is material constant, and m is strain rate sensitivity index, which is defined as follows [41]:

$$m = \frac{\mathrm{d}J}{\mathrm{d}G} = \left| \frac{\mathrm{d}(\ln \sigma)}{\mathrm{d}(\ln \dot{\varepsilon})} \right|_{\varepsilon,T} \tag{13}$$

According to DMM theory [42], the hot-work material system is considered as a nonlinear energy dissipator, which can be characterized by energy dissipation efficiency factors η [43]:

$$\eta = 2m/(m+1) \tag{14}$$

The power dissipation diagram is a contour plot of the power dissipation rate as a function of temperature (T) and strain rate (ε). The area with a high η value may cause dynamic recovery and dynamic recrystallization, which exhibits good processing performance. However, in some cases, there are some unstable zones in high-value areas. Therefore, in order to obtain the optimal thermal processing parameters of the material, it is necessary to calculate the corresponding instability diagram based on the instability criterion. Prasad et al. [44] proposed a rheological instability criterion based on the maximum entropy principle to analyze the materials, as shown in Equation (15):

$$\xi(\dot{\varepsilon}) = \frac{\partial \ln\left(\frac{m}{m+1}\right)}{\partial \ln \dot{\varepsilon}} + m \leq 0 \tag{15}$$

where $\zeta(\dot{\varepsilon})$ is the instability factor. The instability map is the area where the instability factor varies with negative values in the contour map of temperature (T) and strain rate ($\dot{\varepsilon}$). The rheological instability may occur in this area, which should be avoided during processing materials. The processing map is composed of power dissipation diagram and instability map. Figure 9 shows the processing map of $AlCoCrFeNiTi_{0.5}$ HEA with strain at 0.3, 0.4, 0.5 and 0.6. The contour line represents the power dissipation coefficient, and the shaded

area represents the unstable zone. It can be concluded that there is an unstable zone in all figures. When the strain is 0.3, the unstable zone is the area with temperature ranging from 1100 to 1130 K and strain rate ranging from 0.35 to 1 s^{-1}. With the increase in deformation, the unstable area becomes larger. When the strain is 0.6, the unstable zone is the area with temperature ranging from 1073 to 1373 K and strain rate ranging from 0.13 to 1 s^{-1}. Besides all above areas, the region corresponding to the highest energy dissipation rate during deformation is the optimal deformation zone for $AlCoCrFeNiTi_{0.5}$ HEA. It can be seen that the optimal deformation zone is in the temperature range of 1150–1300 K and the strain rate range of 0.002–0.05 s^{-1}.

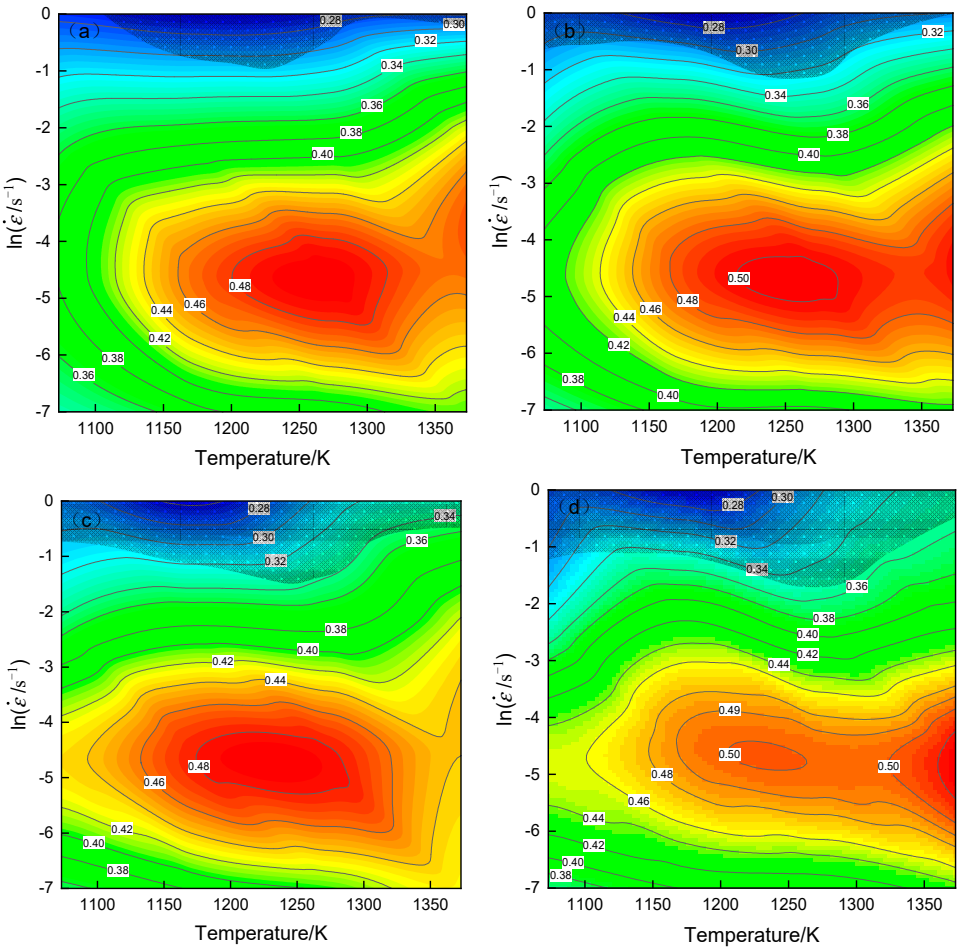

Figure 9. Processing map of $AlCoCrFeNiTi_{0.5}$ HEA with strain at (**a**) 0.3, (**b**) 0.4, (**c**) 0.5 and (**d**) 0.6.

4. Conclusions

(1) Under the conditions of deformation temperature 1073–1373 K, strain rate 0.001–1 s^{-1}, and strain rate 70%, the hot-deformation process of $AlCoCrFeNiTi_{0.5}$ HEA is dominated by a softening mechanism that combines work hardening, dynamic recovery, and dynamic recrystallization. The strain rate and deformation temperature play a significant impact on the stress–strain curve.

(2) The constitutive equation is established and verified, the correlation coefficient is 0.9873, which indicates that the constitutive equation can accurately predict the flow stress of $AlCoCrFeNiTi_{0.5}$ HEA. The constitutive equation of $AlCoCrFeNiTi_{0.5}$ can be expressed as follows.

$$\begin{cases} \sigma = \frac{1}{\alpha}\ln\left\{\left(\frac{Z}{A}\right)^{\frac{1}{n}} + \left[\left(\frac{Z}{A}\right)^{\frac{2}{n}} + 1\right]^{\frac{1}{2}}\right\} \\ Z = \dot{\varepsilon}\exp\left(\frac{Q}{RT}\right) \\ \alpha = -0.3303\varepsilon^6 + 0.6176\varepsilon^5 - 0.3993\varepsilon^4 + 0.0951\varepsilon^3 \\ \quad -0.0036\varepsilon^2 + 0.0058\varepsilon + 0.0028 \\ n = -166.77\varepsilon^6 + 467.09\varepsilon^5 - 505.70\varepsilon^4 + 255.07\varepsilon^3 \\ \quad -51.47\varepsilon^2 - 1.87\varepsilon + 4.32 \\ Q = -53062.40\varepsilon^6 + 131273.29\varepsilon^5 - 127864.15\varepsilon^4 \\ \quad +61133.49\varepsilon^3 - 14029.85\varepsilon^2 + 1015.05\varepsilon + 256.35 \\ \ln A = 6902.09\varepsilon^6 - 17741.01\varepsilon^5 + 18090.01\varepsilon^4 \\ \quad -9345.30\varepsilon^3 + 2614.99\varepsilon^2 - 398.61\varepsilon + 43.03 \end{cases}$$

(3) The processing map is established, and the optimal deformation zone for $AlCoCrFeNiTi_{0.5}$ HEA is in the temperature range of 1150–1300 K with a strain rate range of 0.002–0.05 s^{-1}.

Author Contributions: Conceptualization, T.L. and X.K.; methodology, X.L.; validation, X.L.; formal analysis, Y.W.; investigation, C.Z.; resources, X.L.; data curation, X.L.; writing—original draft preparation, X.L.; writing—review and editing, Y.W. funding acquisition, X.L. All authors have read and agreed to the published version of the manuscript.

Funding: This research was funded by Scientific Research Project of Hunan Provincial Department of Education, grant number 19A126.

Institutional Review Board Statement: Not applicable.

Informed Consent Statement: Not applicable.

Data Availability Statement: All data that support the findings of this study are included within the article.

Acknowledgments: The authors thank the Scientific Research Project of Hunan Provincial Department of Education and Undergraduate Innovation and Entrepreneurship of Hunan Province.

Conflicts of Interest: The authors declare no conflict of interest.

References

1. Zhang, Y.; Zuo, T.T.; Tang, Z.; Michael, C.G.; Karin, A.D.; Peter, K.L.; Lu, Z.P. Microstructures and properties of high-entropy alloys. *Prog. Mater. Sci.* **2014**, *61*, 1–93. [CrossRef]
2. Cantor, B.; Chang, I.T.H.; Knight, P. Microstructural development in equiatomic multicomponent alloys. *Mater. Sci. Eng.* **2004**, *375–377*, 213–218. [CrossRef]
3. Yi, J.J.; Wang, L.; Zeng, L.; Xu, M.; Tang, S. Excellent strength-ductility synergy in a novel single-phase equiatomic CoFeNiTiV high entropy alloy. *Int. J. Refract. Met. Hard Mater.* **2020**, *95*, 105416. [CrossRef]
4. Parakh, A.; Vaidya, M.; Kumar, N.; Chetty, R.; Murty, B.S. Effect of crystal structure and grain size on corrosion properties of AlCoCrFeNi high entropy alloy. *J. Alloys Compd.* **2020**, *863*, 158056. [CrossRef]
5. Bhattacharjee, T.; Wani, I.S.; Sheikh, S.; Clark, I.T.; Okawa, T.; Guo, S.; Bhattacharjee, P.P.; Tsuji, N. Simultaneous Strength-Ductility Enhancement of a Nano-Lamellar $AlCoCrFeNi_{2.1}$ Eutectic High Entropy Alloy by Cryo-Rolling and Annealing. *Sci. Rep.* **2018**, *8*, 3276. [CrossRef]
6. Shabani, M.; Indeck, J.; Hazeli, K.; Jablonski, P.D.; Pataky, G.J. Effect of Strain Rate on the Tensile Behavior of CoCrFeNi and CoCrFeMnNi High-Entropy Alloys. *J. Mater. Eng. Perform.* **2019**, *28*, 4348–4356. [CrossRef]
7. Samoilova, O.; Shaburova, N.; Samodurova, M.; Pashkeev, K.; Moghaddam, A.O.; Doubenskaia, M.; Sova, A.; Trofimov, E. Microstructural evolution of $Al_{0.25}$CoCrFeNi- Cu and $Al_{0.45}CoCrFeNiSi_{0.45}$ high-entropy alloys during laser cladding. *Proc. Inst. Mech. Eng. Part L J. Mater. Des. Appl.* **2022**, *236*, 1806–1813.
8. Liu, Q.; Wang, X.Y.; Huang, Y.B.; Xie, L.; Xu, Q.; Li, L.H. Effect of Mo Content on Microstructure and Corrosion Resistance of CoCrFeNiMo High Entropy Alloy. *Chin. J. Mater. Res.* **2020**, *34*, 868–874.

9. Zhang, A.; Han, J.; Meng, J.; Su, B.; Li, P. Rapid preparation of AlCoCrFeNi high entropy alloy by spark plasma sintering from elemental powder mixture. *Mater. Lett.* **2016**, *181*, 82–85. [CrossRef]
10. Chuang, M.H.; Tsai, M.H.; Wang, W.R.; Lin, S.J.; Yeh, J.W. Microstructure and wear behavior of $Al_xCo_{1.5}CrFe\ Ni_{1.5}Ti_y$ high-entropy alloys. *Acta Mater.* **2011**, *59*, 6308–6317. [CrossRef]
11. Guo, L.; Ou, X.; Ni, S.; Liu, Y.; Song, M. Effects of carbon on the microstructures and mechanical properties of FeCoCrNiMn high entropy alloys. *Mater. Sci. Eng. A* **2019**, *746*, 356–362. [CrossRef]
12. Verma, A.; Tarate, P.; Abhyankar, A.C.; Mohape, M.R.; Gowtam, D.S.; Deshmukh, V.P.; Shanmugasundaram, T. High emperature Wear in CoCrFeNiCux High Entropy Alloys: The Role of Cu. *Scr. Mater.* **2019**, *161*, 28–31. [CrossRef]
13. Qin, G.; Chen, R.R.; Zheng, H.T.; Fang, H.Z.; Wang, L.; Su, Y.Q.; Fu, H.Z. Strengthening FCC CoCrFeMnNi high entropy alloys by Mo addition. *J. Mater. Sci. Technol.* **2019**, *35*, 578–583. [CrossRef]
14. Mohamed, A.H.; Hossam, M.Y.; Ahmed, S.A.M.; Ahmed, E.E.N.; Omayma, A.E. Effect of Copper Addition on the AlCoCrFeNi High Entropy Alloys Properties via the Electroless Plating and Powder Metallurgy Technique. *Crystals* **2021**, *11*, 540.
15. Zhao, P.B.; Zhu, J.P.; Yang, K.J.; Li, M.L.; Shao, G.; Lu, H.X.; Ma, Z.; Wang, H.L.; He, J.L. Outstanding wear resistance of plasma sprayed high-entropy monoboride composite coating by inducing phase structural cooperative mechanism. *Appl. Surf. Sci.* **2023**, *616*, 156516. [CrossRef]
16. Zhao, P.B.; Zhu, J.P.; Li, M.L.; Shao, G.; Lu, H.X.; He, J.L. Theoretical and experimental investigations on the phase stability and fabrication of high-entropy monoborides. *J. Eur. Ceram. Soc.* **2023**, *43*, 2320–2330. [CrossRef]
17. Yu, L.Y.; Wang, C.; Zhu, L.L.; Zhang, H.; Huang, H.L.; Ruan, J.J.; Zhang, S.Z.; Jiang, L.; Zhou, X. Microstructure and properties of AlxCoCrFeNi high entropy alloys fabricated by laser additive manufacturing. *J. Mater. Eng.* **2023**. (In Chinese)
18. Deng, C.; Li, R.D.; Yuan, T.C.; Niu, P.D. Influence of Al Content on Microstructure and Nanoindentation of Selective Laser Melting AlxCoCrFeNi(x = 0.3, 0.5, 0.7, 1.0). *J. Mater. Eng.* **2022**, *50*, 27–35. (In Chinese)
19. Zhang, P.; Wang, S.X.; Lin, Z.Y.; Yue, X.J.; Gao, Y.R.; Zhang, S.T.; Yang, H.J. Investigation on the mechanism of micro-milling CoCrFeNiAlX high entropy alloys with end milling cutters. *Vacuum* **2023**, *211*, 111939. [CrossRef]
20. Wu, Y.; Li, Z.; Feng, H.; He, S. Atomic Interactions and Order-Disorder Transition in FCC-Type FeCoNiAl1-xTix High-Entropy Alloys. *Materials* **2022**, *15*, 3992. [CrossRef]
21. Ye, H.M.; Yang, W.C.; Pang, X.Z. Effect of titanium content on wear resistance of CoCuFeNiVTix high-entropy alloys. *J. Guangxi Univ. (Nat. Sci. Ed.)* **2017**, *42*, 1187–1191.
22. Zhang, L.; Sha, M.H.; Zhang, J.W.; Chen, Z.S.; Li, S.L. Effect of Titanium on the Microstructure and Wear Resistance of AlCoCrFeNiTi0.5 Alloy Coating Prepared by Laser Cladding. *Mater. Prot.* **2022**, *55*, 24–30. [CrossRef]
23. Shun, T.T.; Chang, L.-Y.; Shiu, M.H. Microstructure and Mechanical Properties of Multiprincipal Component CoCrFeNiMox Alloys. *Mater. Charact.* **2012**, *70*, 63–67. [CrossRef]
24. Liu, Z.; Xiong, Z.P.; Chen, X.W. Large-size high-strength and high-ductilityAlCoCrFeNi2.1 eutectic high-entropy alloy produced by hot-rolling and subsequent aging. *Mater. Lett.* **2022**, *315*, 131933. [CrossRef]
25. Savaedi, Z.; Motallebi, R.; Mirzadeh, H. A review of hot deformation behaviorand constitutive models to predict flow stress of high-entropy alloys. *J. Alloys Compd.* **2022**, *903*, 163964. [CrossRef]
26. Gao, P.F.; Fu, M.W.; Zhan, M.; Lei, Z.N.; Li, Y.X. Deformation behavior and microstructure evolution of titanium alloys with lamellar microstructure in hot working process: A review. *J. Mater. Sci. Technol.* **2020**, *39*, 56. [CrossRef]
27. Dong, F.Y.; Yuan, Y.; Li, W.D.; Zhang, Y.; Liaw, P.K.; Yuan, X.G.; Huang, H.J. Hot deformation behavior and processing maps of an equiatomic MoNbHfZrTi refractory high entropy alloy. *Intermetallics* **2020**, *126*, 106921. [CrossRef]
28. Prasad, Y.V.R.K. Dynamic materials model: Basis and principles. *Metall. Mater. Trans.* **1996**, *27*, 235. [CrossRef]
29. Xiao, B.L.; Huang, Z.Y.; Ma, K.; Zhang, X.X.; Ma, Z.Y. Research on hot deformation behaviors of discontinuously reinforced aluminum composites. *Acta Metall. Sin.* **2019**, *55*, 59.
30. Liu, X.B.; Wu, G.L.; Zhou, C.Y. Constitutive modeling of dynamic recrystallization behavior and processing map of Cr5 steel. *J. Cent. South Univ.* **2016**, *23*, 3065–3071. [CrossRef]
31. Jeong, H.; Kim, W.J. Deformation Mechanisms and Processing Maps for High Entropy Alloys (Presentation of Processing Maps in Terms of Zener–Hollomon Parameter): Review. *Materials* **2023**, *16*, 919. [CrossRef] [PubMed]
32. Mcqueen, H.J.; Ryan, N.D. Constitutive analysis in hot working. *Mater. Sci. Eng. A* **2002**, *322*, 43–46. [CrossRef]
33. Trusov, P.; Kondratev, N.; Podsedertsev, A. Grain structure rearrangement by means the advanced statistical model modified for describing dynamic recrystallization. *Metals* **2023**, *13*, 113. [CrossRef]
34. Lin, Y.C.; Chen, M.S.; Zhong, J. Constitutive modeling for elevated temperature flow behavior of 42CrMo steel. *Comput. Mater. Sci.* **2008**, *42*, 470. [CrossRef]
35. Sellars, C.M.; McTegart, W.J. On the mechanism of hot deformation. *Acta Metall.* **1966**, *14*, 1136. [CrossRef]
36. Lin, Y.C.; Wen, D.X.; Deng, J.; Liu, G.; Chen, J. Constitutive models for high temperature flow behaviors of a Ni-based superalloy. *Mater. Des.* **2014**, *59*, 115. [CrossRef]
37. Ferdowsi, M.R.G.; Nakhaie, D.; Benhangi, P.H.; Ebrahimi, G.R. Modeling the high temperature flow behavior and dynamic recrystallization kinetics of a medium carbon microalloyed steel. *J. Mater. Eng. Perform.* **2014**, *23*, 1077–1087. [CrossRef]
38. Ebrahimpourghandi, B.; Mahmudi, R. Hot deformation constitutive analysis and processing maps of the as-cast and wrought Mg-2.5Gd-0.5Zr alloy. *J. Alloys Compd.* **2023**, *942*, 169133. [CrossRef]

39. Prasad, Y.V.R.K.; Seshacharyulu, T. Modelling of hot deformation for microstructural control. *Int. Mater. Rev.* **1998**, *43*, 243. [CrossRef]
40. Sun, F.C.; Li, J.S.; Han, J.K.; Peng, Y.H.; Zhou, K.; Chen, L.J.; Cao, X. Hot deformation behavior and processing map of AlFeCoNi-Mo0.2 high-entropy alloy. *J. Netshape Form. Eng.* **2021**, *13*, 91–97. (In Chinese)
41. Sumit, G.; Mahesh, C.S.; Daria, S.; Suhrit, M. Elucidation of deformation mechanisms and construction of processing maps for a Ti+Nb stabilized IF steel. *Mater. Sci. Eng. A* **2020**, *790*, 139648.
42. Lou, Y.; Chen, H.; Ke, C.X.; Long, M. Hot tensile deformation characteristics and processing map of extruded AZ80 Mg alloys. *J. Mater. Eng. Perform.* **2014**, *23*, 1904–1914. [CrossRef]
43. Sui, D.S.; Wang, T.; Zhu, L.L.; Ga, L.; Cui, Z.S. Mathematical modeling of high-temperature constitutive equations and hot processing maps for as-cast SA508-3 steel. *JOM* **2016**, *68*, 2944–2951. [CrossRef]
44. Prasad, Y.V.R.K.; Gegel, H.L.; Doraivelu, S.M.; Malas, J.C.; Morgan, J.T.; Lark, K.A.; Barker, D.R. Modeling of dynamic material behavior in hot deformation: Forging of Ti-6242. *Metall. Trans.* **1984**, *15*, 1883. [CrossRef]